Planar Prism Spectrometer based on Adiabatically Connected Waveguiding Slabs

F. Civitci[a,b,*], M. Hammer[a,c], and H.J.W.M. Hoekstra[a]

[a]MESA+ Instute for Nanotechnology, University of Twente, Enschede, 7522NB, The Netherlands
[b] Department of Electronics and Communication Eng., Istanbul Technical University, Istanbul, 34469, Turkey
[c] Department of Theoretical Electrical Engineering, University of Paderborn, 33098, Germany

Abstract **-** The device principle of a prism-based on-chip spectrometer for TE polarization is introduced. The spectrometer exploits the modal dispersion in planar waveguides in a layout with slab regions having two different thicknesses of the guiding layer. The set-up uses parabolic mirrors, for the collimation of light of the input waveguide and focusing of the light to the receiver waveguides, which relies on total internal reflection at the interface between two such regions. These regions are connected adiabatically to prevent unwanted mode conversion and loss at the edges of the prism. The structure can be fabricated with two wet etching steps. The paper presents basic theory and a general approach for device optimization. The latter is illustrated with a numerical example assuming SiON technology.

Keywords **-** Goos Hänchen Shift, Integrated Optics, Optical Imaging, Optical Waveguides, Prism Spectrometers, Total Internal Reflection Mirrors

1. INTRODUCTION

In the early years (70's) of Integrated Optics (IO), the theory and experimental characterization of slab waveguide based components, such as thin film lenses, prisms, reflectors and polarization splitters were extensively investigated [1]. The design of these components is straightforward since the propagation of light waves in these slabs can be described by geometrical optics in 2D and diffraction theory [2]. Furthermore, slab waveguide fabrication is not a complicated process. In spite of these advantages, only a small number of device principles, which combines one or more of these components, have been implemented, like prism based mode separators [3], grating based de-multiplexers [4] and thermo-optic switches [5].

Wavelength (de)multiplexing planar devices, or micro-spectrometers, have a large potential for applications in telecommunication and sensing [6-10]. In planar implementations the device principle is often based on IO variants of bulky grating spectrometers like an arrayed waveguide grating (AWG) [6], employing diffractionless propagation in waveguides and compact Echelle gratings [9, 10]. In addition, cascaded Mach-Zehnder interferometers and ring resonators are being used [11, 12] as micro-spectrometers. In particular, the AWG is quite often applied owing to its robustness and high resolution compared to the device area. The latter is related to the working principle of the device based on the use of higher diffraction orders, which also leads, as a possible disadvantage, to spectral overlap (limited free spectral range) and loss via spreading of the intensity over a number of orders. The advantages of employing a prism-based spectrometer are the absence of extra diffraction orders (no power splitting) and an unlimited free spectral range.

In this paper, we describe the performance and design aspects of a miniature prism spectrometer, which can be fabricated in a relatively simple way with adiabatically connected slab waveguides (having two different thicknesses), using in the design principles of geometrical optics and diffraction theory. In such a spectrometer dispersion is introduced by the differing wavelength dependence of the effective indices of the modes in thin and thick films. The device relies on ridge waveguides for light transport and on parabolic mirrors for collimation and focusing. A design strategy will be presented and illustrated via a numerical example with TE polarized light in a range of 100 nm around the central wavelength of λ_c = 850 nm with a channel spacing of 5 nm by using SiON waveguide technology.

The rest of this paper is organized as follows. First, we will introduce the principle and basic theory related to the prism spectrometer in Section 2. The part of the imaging theory discussed in this section is well usable for other integrated optics based spectrometer types, such as AWGs. It is followed by an explanation of the design of this device in Section 3, where also a numerical example is given. The paper ends with conclusions in Section 4. A preliminary account of this design strategy has been given in [13].

* Corresponding author at Department of Electronics and Communication Eng., Istanbul Technical University, Istanbul, 34469, Turkey. E-mail: fehmi.civitci@gmail.com, Tel: +90 212 2853613.

2. PRISM SPECTROMETER: PRINCIPLE AND BASIC THEORY

A schematic picture of the considered prism spectrometer device is shown in Fig. 1. It is composed of an input waveguide, a collimating mirror, a prism slab, a focusing mirror and receiver waveguides, corresponding to different wavelengths. The picture in the middle of Fig. 1 with output of 3 adjacent waveguides shows the important spectrometer parameters that will be used in this paper, such as 3 dB bandwidth ($\Delta\lambda$), channel spacing ($\Delta\lambda_{cs}$), adjacent channel cross-talk (ACCT), global cross-talk (CT) and Loss.

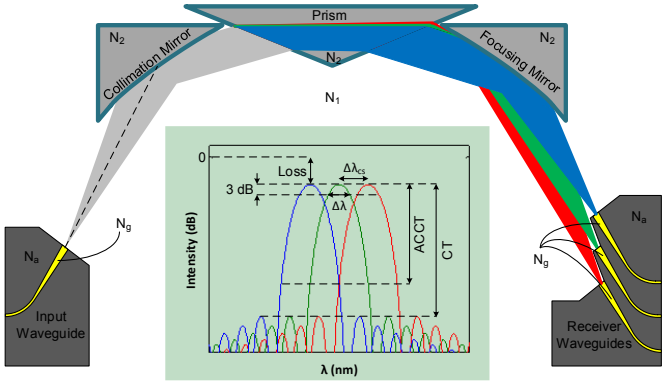

Fig. 1. Schematic of the considered prism spectrometer. The white and dark grey areas correspond to thick and thin slabs, respectively. Ridge waveguides are indicated by yellow lines. The inset illustrates schematically the relation of the output intensities to the parameters that characterize the device performance. Regions with different thicknesses of the guiding layer are connected adiabatically via vertical tapering.

The proposed device is planned to be implemented in SiON waveguide technology by using a stoichiometric Si_3N_4 (nitride) layer sandwiched between buffer and cladding SiO_2 (oxide). Patterning of nitride will be done by using a BHF wet etching process, which has a very low etch rate being 0.9 nm/min [14] and so very controllable etching performance, in two different process steps; (i) definition of input/output waveguides and (ii) definition of prism and mirror trenches. A sacrificial oxide layer is deposited on top of the nitride layer in the latter in order to achieve the adiabatic transition on the edges of patterned structures. The main advantage of using an adiabatic transition of the layer thickness, and thus the effective refractive index, between the slab waveguides is the elimination of partial reflection of the incident light at the edges of the prism [1]. With such a tapering the angle of incidence to the prism can be chosen relatively high (just below the critical angle θ_{crit}), which is beneficial for a larger angular dispersion (enabling a smaller device area for a given resolution) as discussed below (Section 2.1), without increasing insertion loss and the amount of stray light in the spectrometer. These adiabatic transitions also affect the modal phase shift upon total internal reflection (TIR) by the mirrors and so the imaging onto the receiver waveguides. This will be elaborated in Section 2.4. In the following subsections we will present the basic theory for the set-up, relevant for device design and operation.

2.1 Prism

A sketch of the prism is shown in Fig. 2, where also the ray trajectory is indicated and used symbols are introduced.

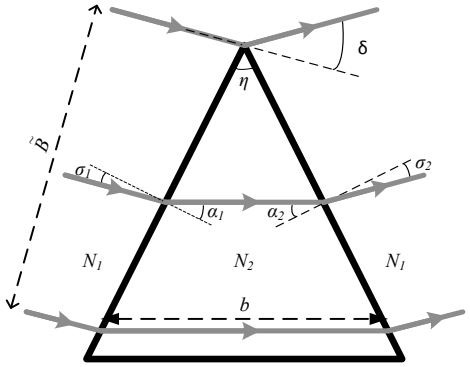

Fig. 2. Schematic (top view) of a generic prism structure.

The angular dispersion is defined by

$$\sigma_2' = \partial\sigma_2/\partial\lambda, \tag{1}$$

where λ is the (vacuum) wavelength. The angular dispersion can be rewritten as follows: Diffraction at the prism interfaces is governed by Snell's law. For the first interface, this can be written as

$$\sin\sigma_1 = D\sin\alpha_1, \tag{2}$$

where we defined $D = N_2/N_1$, with N_1 and N_2 the effective indices of the thick and thin slabs, respectively. Note that the following inequality holds for $N_2 < N_1$. Knowing that σ_1 does not depend on λ, the derivative of Eq. (2) gives

$$\alpha_1' = -\frac{D'}{D}\tan\alpha_1, \tag{3}$$

with $D' = \partial D/\partial\lambda$. The relation between α_1 and α_2 can be found from the geometry leading to

$$\alpha_1 + \alpha_2 = \eta. \tag{4}$$

By combining Eqs. (3) and (4) we arrive at

$$\alpha_2' = \frac{D'}{D}\tan\alpha_1. \tag{5}$$

If Snell's law is applied to the second interface it follows

$$\sin\sigma_2 = D\sin\alpha_2, \tag{6}$$

from which the following can be obtained by taking the derivative,

$$\sigma_2' = D'\frac{\sin\alpha_2}{\cos\sigma_2} + D\alpha_2'\frac{\cos\alpha_2}{\cos\sigma_2}. \tag{7}$$

The above equality can be rewritten by inserting Eqs. (5) into (7) as follows:

$$\sigma_2' = D'\left(\frac{\sin\alpha_2}{\cos\sigma_2} + \frac{\sin\alpha_1\cos\alpha_2}{\cos\alpha_1\ \sin\sigma_2}\right). \tag{8}$$

For later use we consider the angular dispersion, assuming minimum deviation ($\alpha_1 = \alpha_2, \sigma_1 = \sigma_2 = \sigma$), which can be re-written from Eq. (8) into:

$$\sigma_2' = \frac{D'}{D}(\tan\sigma + 1). \tag{9}$$

The deviation angle δ can be expressed as

$$\delta = \eta - \sigma_1 - \sigma_2 = \alpha_1 + \alpha_2 - \sigma_1 - \sigma_2, \tag{10}$$

where we used Eq. (4). The minimum deviation condition implies $\partial(\sigma_1 + \sigma_2)/\partial\sigma_1 = 0$, or $\partial\sigma_2/\partial\sigma_1 = -1$. As a consequence of the latter relative angles don't change, for light at a certain wavelength with an angle of incidence near σ_1, traversing the prism. Consequently, beams don't change shape while traveling through the prism, provided that there is no truncation of the beam (by the limited dimensions of the prism) and the angular dependence of the transmission is small (as accomplished by the adiabatic transitions; see Section 3 for a numerical example). So, if a Gaussian beam having a transverse field distribution according to

$$A(\rho) = A_1 e^{\left(-\rho^2 2\ln 2/W^2\right)}, \tag{11}$$

with W the full width at half maximum (FWHM) and ρ the transverse coordinate, is traversing the prism its shape will be unaltered if truncation of the beam by the limited prism size can be neglected. The far field of that beam is then given by [15]

$$F(u) = \int_{-\infty}^{+\infty} A(\rho) e^{iu\rho} d\rho = F_0 e^{-u^2 2 \ln 2/\Delta u^2}, \quad (12)$$

where we assumed a time dependence $\exp(i\omega t)$ of all electromagnetic fields, and u is defined as $u \equiv kN_1 \sin\phi$ with k the wavenumber and ϕ the diffraction angle. The FWHM of the far field intensity is given by $\Delta u = 4 \ln 2 / W$ and corresponds to $\Delta\phi = \Delta u/(kN_1)$. An expression for the resolution can now be derived as follows. Assuming that two equally shaped peaks corresponding to different wavelengths are resolved if these are separated by the FWHM it follows

$$\Delta\phi = \sigma_2' \Delta\lambda_f, \quad (13)$$

$$\Delta\lambda_f = 4 \ln 2 / (\sigma_2' W k N_1). \quad (14)$$

In the above $\Delta\lambda_f$ is the FWHM of the far field intensity, assuming that it is not affected by truncation of the Gaussian beam due to the finite size of the prism (or mirrors). As will be discussed in Section 2.3 truncation effects are almost negligible if the truncation parameter ς is larger than ~3, with ς defined by $\tilde{B} = \varsigma W$ ($\tilde{B}$ is the width of the output/input beam as defined in Fig. 2). If we assume, for example, that $\varsigma = 4$, substitute $\tilde{B} = \varsigma W$ into Eq. (14) it follows from the geometry, with $D' \equiv \partial D/\partial\lambda$:

$$\Delta\lambda_f = \frac{8 \ln 2 D}{D' \tilde{B} k N_1 (1 + \tan\sigma)}, \quad (15)$$

where $\sigma \equiv \sigma_1 = \sigma_2$ and $\alpha_1 = \alpha_2$, assuming the minimum deviation condition. It is seen from the above that σ should be chosen as large as possible for a smaller device area (so for smaller $\tilde{B}$) and thus optimization of the resolution for given beam width, $\tilde{B}$), comes down to optimizing the quantity $R = N_1 D'/D$.

It is seen from eq. 9 that for a large angular dispersion (and so for higher resolution) the angle of incidence on the prism facet should be as large as possible (analogue to what we concluded above using Eq. (15)). On the other hand it should of course not exceed the critical angle for TIR, θ_{crit}, defined by

$$\theta_{crit} = \sin^{-1}(N_2/N_1). \quad (16)$$

It is found, as illustrated in Section 3 with an example, that with proposed adiabatic transitions between areas with a thick and a thin guiding layer there is an abrupt transition from very low reflectance at angles of incidence below θ_{crit} to (of course) full reflectance for angles of incidence above θ_{crit}. This can be employed by choosing

$$\sigma \leq \theta_{crit}, \quad (17)$$

such that σ_2 is below θ_{crit} for the whole considered wavelength region. For later use we give the inequality holding at minimum deviation

$$\partial\delta/\partial\sigma|_{MD} > 0, \quad (18)$$

which can be derived using the definition for δ and Snell's law (Eq. (1)) together with the inequality $N_2 < N_1$.

2.2 Mirror

Both mirrors, which are identical owing to the assumed symmetric implementation, are parabolic mirrors, which can be designed using Fermat's principle. Fig. 3(a) shows the schematic of a parabolic collimation/focusing mirror, which has a collimated beam parallel to the *x*-axis. In this figure θ_l and θ_h are the incidence/reflection angles for the start and end points of the mirror respectively, $\tilde{B}$ is the width of the output/input beam and γ ($= 2\theta_h - 2\theta_l$) is the angle between the outermost rays and the focal point is chosen to be origin. Fermat's principle dictates that the total optical path lengths between the focal point and points at an arbitrary cross section of the collimated beam, say, at $x = x_h$, are all the same. Denoting the mirror coordinates by (*x*,*y*) it follows:

$$\sqrt{x^2 + y^2} + (x_h + x) = d_0, \quad (19)$$

which can be rewritten by defining a new variable $c_m \equiv d_0 - x_h$ $\mathrm{c_m = d_o\text{-}x_n}$ as

$$\sqrt{x^2 + y^2} - x = c_{\mathrm{m}}. \tag{20}$$

Next we will show, for later use, that the parabolic mirror (shape and size) is fully defined by the quantities $\tilde{B}$, θ_l and γ. Using Eq. (20) and the relation

$$y = -x \tan(2\theta)\,, \tag{21}$$

where θ is the incidence angle of an arbitrary point on the mirror, it follows (assuming that $\cos(2\theta) < 0$, as in the device considered by us in section 3.2)

$$x\left(\sqrt{1 + (\tan(2\theta))^2} - 1\right) = -\frac{x[1 + \cos(2\theta)]}{\cos(2\theta)} = c_m, \tag{22}$$

which enables us to write:

$$x = \frac{x_l[1 + \cos(2\theta_l)]\cos(2\theta)}{[1 + \cos(2\theta)]\cos(2\theta_l)}. \tag{23}$$

Then, with Eq. (21) and $y_h = y_l + \tilde{B} = -x_h \tan(2\theta_h)$ we find

$$y_l = -\tilde{B} - x_h \tan(2\theta_h) = -x_l \tan(2\theta_l). \tag{24}$$

Substitution of x_h according to Eq. (23), with $(x, \theta) = (x_h, \theta_h)$, into the second equality of Eq. (24) leads after simple manipulations to:

$$\tilde{B} = -2\cos\theta_l \sin(\gamma/2)\, x_l/(\cos(\theta_l + \gamma/2)\cos(2\theta_l)), \tag{25}$$

from which the full mirror curve can indeed be derived, also using Eqs. (23) and (21).

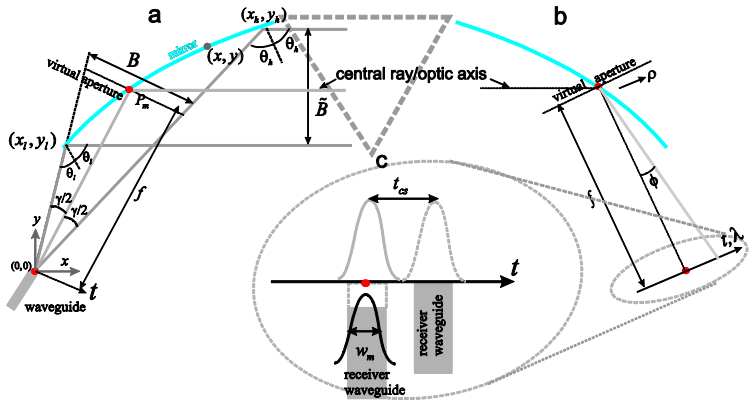

Fig. 3. Schematic pictures of the collimation mirror (a), the focusing mirror (b) and the focal area (c), introducing the used symbols.

In order to obtain a simplifying picture of the working of the mirror a virtual aperture and a focal length are introduced (see Fig. 3(a) and (b)). The former is defined by a line piece through the point P_m, which is the intersection point of the bisector of the outermost rays and the mirror curve, perpendicular to the corresponding ray and with end points defined by the (extrapolated) outermost rays. The distance between point P_m and the focus is called f, the focal length. The width of the virtual aperture, B, is equal to the (maximum) beam width, $\tilde{B}$, with a small relative error proportional to γ^2. Note that the point P_m of the collimation mirror (as well as of the focusing mirror) is chosen to be on the optical axis and that it does not correspond to the middle of the parallel beam coming from the input mirror. As a consequence, assuming a symmetrical mode coming from the input waveguide, the field in the collimated beam will be (slightly) asymmetric. But, the asymmetry of this beam (which travels without changing shape through the prism) is fully compensated by the identical focusing mirror. So, for a certain wavelength, the image of the input field near the receiver waveguides can be considered as the focused far field of the input field, truncated by the mirror owing to a finite (virtual) aperture, as defined by the size of the mirror.

The mirror is designed for the central wavelength λ_c. Light at a nearby wavelength is diffracted by the prism and focusing mirror at a different angle. The latter leads to a small change in focal distance, as indicated in Fig. 1, and to aberrations, as follows from numerical calculations using ray tracing according to geometrical optics, corresponding to small blurring of the central spot. It is found from geometrical optics that the blurring effect becomes smaller for smaller angles of incidence θ (which then should be chosen to be just above the critical angle) and smaller values of the angle γ.

2.3 Imaging of the Input Field

We consider the propagation through the prism spectrometer of the modal field at a certain wavelength, λ_0, launched by the input waveguide. In case of ideal lensing and no truncation by the prism (or mirrors) the light is imaged onto the focal line without any change of shape and at a position according to its wavelength. The imaging process, now including the truncation, can be described numerically by taking the Fourier transform of the transverse distribution of the launched field (to calculate the far field), truncation of the far field, taking the complex conjugate of the result (to account for the lensing effect) followed by again taking the Fourier transform. The above can be expressed analytically as follows. The transverse distribution of the far field of the launched mode, E_m is given by [15]

$$F(u) = \frac{1}{\sqrt{2\pi}} \int_{-\infty}^{\infty} E_m(t) e^{iut}\, dt, \tag{26}$$

where $u \equiv kN_1 \sin\phi$, t is a local coordinate and ϕ is the diffraction angle. The shape of the field E_m is defined by the V parameter [16] given by

$$V = kh\sqrt{N_g^2 - N_a^2} \tag{27}$$

with h the width of the waveguide and N_g and N_a are the effective indices of the planar structures corresponding to the guiding and adjacent waveguide sections, respectively. The image in the focal area then follows from [15]

$$E_{im}(t) = \frac{1}{\sqrt{2\pi}} \int_{-\varsigma\Delta u/2}^{\varsigma\Delta u/2} F^*(u) e^{iut}\, du \tag{28}$$

with Δu the FWHM of $|F(u)|^2$ and ς is the truncation parameter. The following relations hold:

$$B\left(= \tilde{B}\right) = \varsigma W = \varsigma f \Delta u, \tag{29}$$

with W the FWHM of the far field intensity. A few numerically computed examples of $|E|^2$ and $|E_{im}|^2$, with maxima assumed at $t = 0$, are given in Fig. 4, using $\varsigma = 3$ and $V = 2$, 4 and 6. The side lobes in the imaged intensities are due to the truncation by the prism and mirrors. The relative power of the light at a certain wavelength captured by a receiver waveguide at a transverse distance t from the center of the image is given by [16]:

$$O(t) = \frac{\left|\int_{-\infty}^{\infty} E_m(t') E_{im}(t'-t)\, dt'\right|^2}{\left|\int_{-\infty}^{\infty} E_m^2(t')\, dt'\right|^2}. \tag{30}$$

Results are given in Fig. 5(a) and Fig. 5(b) for $\varsigma = 2$ and 3 and $V = 2$, 4 and 6, showing the quantity O as a function of t/w_O, with w_O the FWHM of O. Fig. 5(c) shows the computed curves of $w_O\, V/h$ versus V. It is seen that for given index contrast (defined by V/h; see Eq. (27)) w_O increases approximately linearly with V. For comparison, the corresponding modal width (corresponding to the FWHM of $|E_m|^2$), in terms of $w_m\, V/h$, is also shown. As expected w_O is larger than w_m, approximately by a factor of $\sqrt{2}$, as would have been the case if E_m would be purely Gaussian and there would be no truncation.

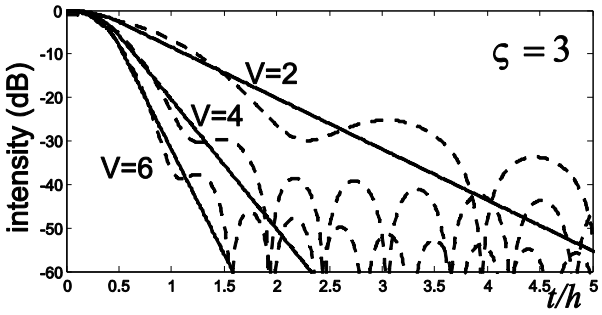

Fig. 4. Intensity profiles for modal fields (solid lines) and the corresponding images (dashed lines) for indicated parameters, calculated using the expression in (28).

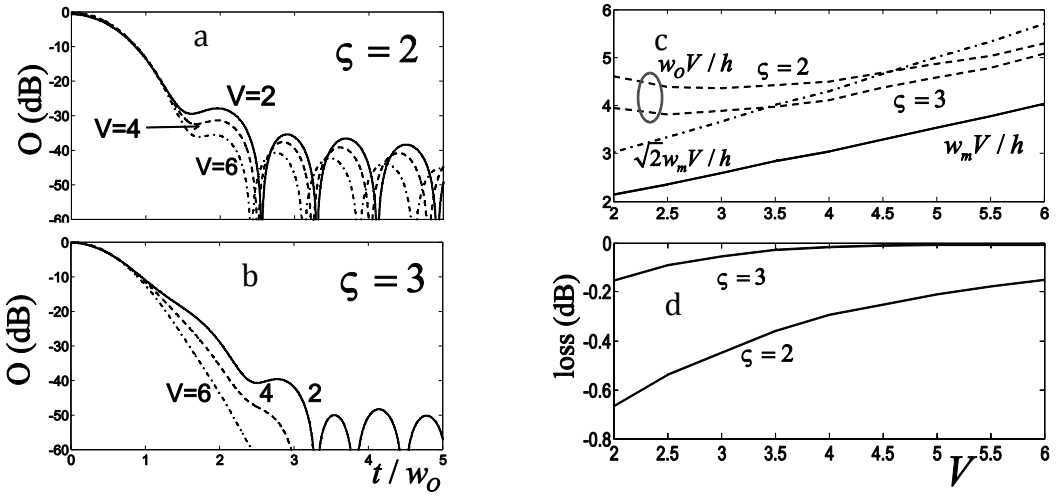

Fig. 5. Relative power captured by a receiver waveguide at a distance of t/w_O from the maximum of the image for (a) ς=2 and (b) ς=3 and modal width, FWHM of O (c) and the functional loss (d) O (t=0) as a function of V.

The functional loss $\left(O(t=0)\right)$, as depicted in Fig. 5(d), is relatively low for considered parameter range. Curves like the ones depicted in Fig. 5 can be used to determine a number of device parameters as follows. The maximum of the image of $|E_{im}^2(t)|$ corresponds to $t=0$ for, say, λ_0. Then, the maximum of the image corresponding to $\lambda_0+\Delta\lambda/2$ (with $\Delta\lambda$ the 3dB bandwidth) should correspond to $t=t_{3dB}=w_O/2$. Knowing the required ratio $\Delta\lambda_{cs}/\Delta\lambda$, the position t_{cs} of the adjacent channel can be obtained from

$$t_{cs}=\Delta\lambda_{cs}w_O/\Delta\lambda \tag{31}$$

where the value of w_O can be determined as explained below. Next, the desired ACCT as well as the global functional CT (owing to the side lobes) can be obtained by selecting the appropriate parameters ς and V from curves as in Fig. 5, assuming for the moment that there are no constraints on the acceptance angle γ (a large acceptance angle may cause blurring of the focal image as noted in section 2.2). For example, if $\Delta\lambda_{cs}/\Delta\lambda=2$ (corresponding to $t_{cs}/w_O=2$ according to Eq. (31)) and if it is required ACCT$<-30dB$ one may choose V slightly larger than 2 ($V=2.2$) with $\varsigma=3$, if the corresponding global CT ($-50dB$) is acceptable. A choice of $V=3$ with $\varsigma=2$ is also an option. If the required ACCT and CT are not attained one may choose for a smaller 3 dB bandwidth than required. One may choose among the above options by considering also the device area as discussed in Section 3. Knowing ς and V one can find h (for given contrast and wavelength, using Eq. (27)), E_m, E_{im}, w_O and the channel spacing, t_{cs}, using Eq. (31). The required focal distance f follows from $w_O=f\sigma_2'\Delta\lambda$ (which follows from the fact that $t_{3dB}=w_O/2$ should correspond to $\lambda_0+\Delta\lambda/2$), and is is given by

$$f=w_O/(\sigma_2'\Delta\lambda). \tag{32}$$

Knowing also f the fields at the virtual aperture can be calculated, the FWHM of the corresponding intensity, W, and so $\tilde{B}$, via $\tilde{B}=\varsigma W$.

2.4 Effects of variations of the Phase Shift upon Reflection

As is well known on TIR of a planar mode by a mirror a phase shift upon reflection (PSR) will occur which depends on structural properties, wavelength and angle of incidence. For light incident on the parabolic mirror in considered set-up, with varying angle of incidence, this means that the PSR is position dependent and these variations along the mirror lead to both (extra) beam deflection and (de)focusing effects for which we will present useful expressions next. In addition to the latter the well-known Goos-Hänchen shift (GHS) [16], originating from the dependence of the PSR on the angle if incidence, should also be taken into account. Below we will present a derivation of expressions for the effect of the variation of the PSR along the mirror surface considering a small, straight mirror section. Next to that the well-known expression for the GHS will be given.

We assume a position dependent PSR, $\varphi(s)$, with s a local coordinate directed along the mirror, and modal reflection coefficient $r = |r|e^{i\varphi}$, for a flat non-uniform (via $\varphi = \varphi(s)$) mirror (see Fig. 6). The figure shows an incoming plane wave, at an angle of incidence θ, represented by two rays (ray 1 and ray 2). Due to the dependence of the PSR, φ, on s the wave is refracted by the mirror at a slightly different angle θ'. The phase changes corresponding to trajectories 1 and 2 in between the dashed lines (indicating the wave fronts) should be equal, so

$$-\Delta s k N_1 \sin\theta + \varphi_1 = -\Delta s k N_1 \sin\theta' + \varphi_2. \tag{33}$$

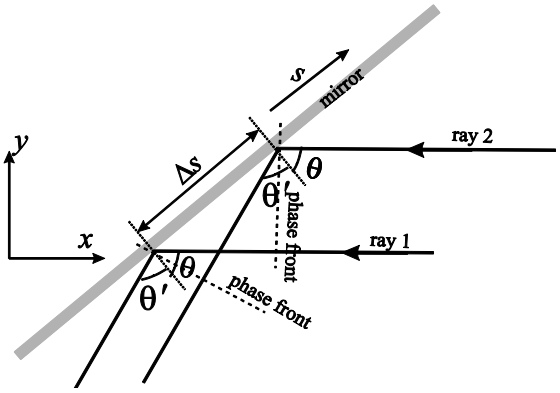

Fig. 6. Illustration to the derivation of the effects of the position dependence of the phase shift upon reflection.

In Eq. (33) the minus sign in front of the phase shifts originating from propagation length stems from the assumed time dependence $\exp(i\omega t)$. From Eq. (33) one may derive

$$\Psi(\theta) \equiv \theta' - \theta = \frac{\partial\varphi}{\partial s}\frac{1}{kN_1\cos\theta} = \frac{\partial\varphi(\theta)}{\partial y}\frac{1}{kN_1}, \tag{34}$$

with Ψ the deflection angle, which varies along the mirror. It can be expanded according to

$$\Psi = \Psi_m + \chi(\theta - \theta_m) + \cdots, \tag{35}$$

where Ψ_m and $\chi \equiv \partial\Psi/\partial\theta$ are both evaluated (numerically) at $\theta_m \equiv (\theta_l + \theta_h)/2$. The first term at the right hand side of Eq. (35) corresponds to a uniform deflection leading to both a small angular shift of the focal point and a change in focal distance (as follows from geometrical optics). The second term leads to a change of the focal distance.

The GHS leads to an apparent shift of the reflected ray along the reflecting interface, given by [16]:

$$GHS = \frac{\partial\varphi}{\partial\theta}\frac{1}{kN_1\cos\theta}. \tag{36}$$

In calculations based on ray tracing one should take into account the effect of the angle and position dependence of the PSR and use both the expressions for GHS (Eq. (36)) and for the tilt (Eq. (34)) to simulate a ray reflected by a curved mirror.

As an alternative to the above approach (in which the effects of variations of the PSR are considered) one could shape the parabolic mirror via numerical calculations such that the above effects are fully compensated

(for the central wavelength λ_c). In order to obtain the magnitude of the PSR one could most conveniently use existing software for channel mode solving, as illustrated by the example in section 3.2.

3. DESIGN

In this section we will first sketch a general optimization strategy for our device on the basis of the theoretical considerations given above. Thereafter, the scheme will be applied for the design of an actual device as an illustration. As mentioned above, only the case of minimum deviation (for the central wavelength, λ_c), corresponding to a symmetric set up, will be considered.

It is assumed that the wavelength channel spacing $\Delta\lambda_{cs}$ and the 3 dB band width ($\Delta\lambda$) are fixed, as well as the maximum allowable ACCT and CT, and that it is our task to design the device such that the device area G (apart from the waveguides) is minimized. As a reasonable measure for G we will take the following approximate expression (see also Fig. 7; G corresponds to the grey rectangle):

$$G \approx f^2 \sin(2\vartheta) + bf\cos\vartheta, \quad 2\vartheta \equiv 4\theta_l - \pi - \delta. \tag{37}$$

Here $\delta\ (= \eta - 2\sigma)$ is the deviation angle and we assumed in Fig. 7 that $\vartheta > 0$ (typically $\vartheta \approx 20^\circ$). It is seen from the equation that f, occurring in both terms, has a slightly larger impact on the device area than base length b. With $\vartheta \approx 20^\circ$ and assuming that b is smaller or not very much larger than f it can be shown from Eq. (37) that the area becomes smaller if δ increases, i.e., $\partial G/\partial\delta < 0$.

As is also seen from Eq. (37), the orientation of the prism has a considerable impact on the device area, as with the opposite orientation $-\delta$ would have to be replaced by $+\delta$, which would lead to a much larger value for ϑ and so for G. In most practical cases (like in the example discussed in Section 3.2) the orientation has to be chosen as indicated in Fig. 7 to attain a lower device area.

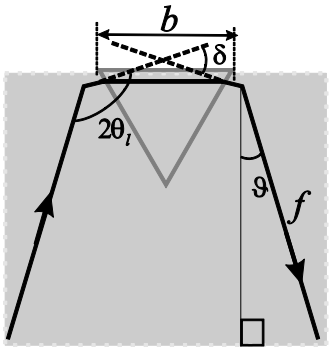

Fig. 7. Illustration to Eq. (37) giving the approximate device area (indicated by the grey rectangle).

3.1 Scheme

The optimization scheme proceeds along the following steps, for which it is assumed that the materials for guiding, cladding and cover layers have been chosen already. The required values for λ_c, $\Delta\lambda_{cs}$, $\Delta\lambda$, the ACCT and the CT are assumed to be given. It is also assumed that the effective index contrast for the ridge waveguide has been chosen.

1. Choose the two thicknesses (h_1 and h_2) for the thick and thin slabs (corresponding to N_1 and N_2, respectively) such that the quantity R (defined in Section 2) is maximized, taking into account, if required, constraints defined by the technology. According to Eq. (15) a larger R leads to a larger resolving power for given lay-out (and so to a lower required device area for given required resolving power). The above choice determines the quantities N_1, N_2, D' and D as well as the critical angle θ_{crit} (see Sec. 2).

2. Determine the angles σ, η and θ_l. Inspecting Eq. (9), it follows that σ should be as large as possible for a larger value of σ_2' and so a smaller value of $\tilde{B}$ (and so a smaller device area), according to Eq. (15), for fixed $\Delta\lambda_f$. On the other hand the angle σ should be below the critical angle, θ_{crit} for small reflection loss at the prism boundaries. The choice of σ may be checked with (approximate) calculations of this loss as in the example below. Knowing σ the angle η of the prism is defined according to Eq. (2) and the property $\eta = \alpha_1 + \alpha_2$. The angle θ_l should be chosen above θ_{crit} for 100% modal reflection but not too far above θ_{crit} to avoid the aberrations mentioned in Section 2.2.

3. Determine the parameters V and ς such that the required device performance is obtained with minimum device area, using graphs like the ones in Fig. 5. On doing so, one may use that $b \propto \varsigma$ and that $f \propto w_O \propto V$ (if

$V \geq 4$) as is seen from Eq. (32) and Fig. 5(c). Note also that generally a smaller ς leads to larger functional losses according to Fig. 5(d). Next, from V and ς one may determine $\tilde{B}$ and f via the procedure outlined in Section 2.3. The quantities $\tilde{B}$, η and σ determine the prism size and shape. Using $\tilde{B} = f\gamma$ fixes the angle γ and so, with θ_l and $\tilde{B}$ the parabolic mirrors. The orientation of the mirrors with respect to the prism follows from the angle σ.

4. The positioning of the input and receiver waveguides can now be calculated with the mirror parameters and geometrical optics, including the PSR effect, as discussed in section 2.4.

5. It has to be checked if the thus obtained device structure leads to (too large) aberrations (as an effect of the parabolic mirrors) for the outermost wavelengths of considered region. If so a larger V value has to be chosen implying a lower acceptance angle for the mirrors and lower aberrations; the adaptation will generally lead to (harmless) over-performance with respect to ACCT and CT.

It is noted from the discussions in Section 2.3 and above that, for given $\Delta\lambda_{cs}/\Delta\lambda$ and ACCT, both f and b are inversely proportional to the 3 dB bandwidth $\Delta\lambda$ and so that G, is roughly inversely proportional to $\Delta\lambda^2$.

3.2 A Numerical Example

The spectrometer that will be discussed in this section is planned to be used for determining the natural moisturizing factor (NMF) in human skin [7]. This application requires a value for $\Delta\lambda_{cs}$ of 5 nm at $\lambda_c = 850\ nm$ with an operating bandwidth of 100 nm. The device will be operated with TE polarization. We assume a 3 dB bandwidth of $\Delta\lambda = 2.5\ nm$, implying that $\Delta\lambda_{cs}/\Delta\lambda = 2$, and values for the cross talk as follows: ACCT $< -40\ dB$ and CT $< -50\ dB$. The guiding layer will be a Si_3N_4 layer (index 2.008), which is sandwiched between two SiO_2 layers (index 1.452). The height of the input/output waveguides is chosen equal to that of the thicker slab waveguide in order to decrease the losses at the exit of the input waveguide and entrance of the receiver waveguides. The ridge height is chosen such that the lateral index contrast of the waveguide is 0.01, which is sufficiently small to arrive at single mode waveguides with the available fabrication processes (minimum feature size 1 μm).

The desired spectrometer is designed by following the optimization scheme explained in the previous section.

1. The quantities N_1 and D' depend on the thicknesses used for the two waveguiding slab regions. We have optimized R by varying the two slab thicknesses between 40 nm, which is a safe lower limit to prevent leakage to the Si substrate, and 170 nm, which is a safe upper limit for the thickness of the Si_3N_4 layer made with our fabrication facility (there may be cracks in the layer if the thickness exceeds 170 nm). As can be seen from Fig. 8, R is maximized to a value of $2.34\ x\ 10^{-4}\ /nm$ by choosing a thickness of 170 nm, which corresponds to N_1 = 1.6931 at λ_c, for the thicker layer (field outside the prism) and a thickness of 40 nm, which corresponds to N_2 = 1.4785 at λ_c, for the thinner layer (prism). Note that, as is seen from Fig. 8, the optimum thickness for the thicker layer would have been 190 nm if there would be no upper limit for the thickness of the Si_3N_4. The height of the Si_3N_4 waveguides is chosen to be 170 nm, which corresponds to N_g (= N_1) = 1.6931 and the ridge height is chosen as 7 nm, which corresponds to N_a = 1.6831. The critical angle corresponding to the two slab regions is given by $\theta_{crit} = 60.84^{\circ}$.

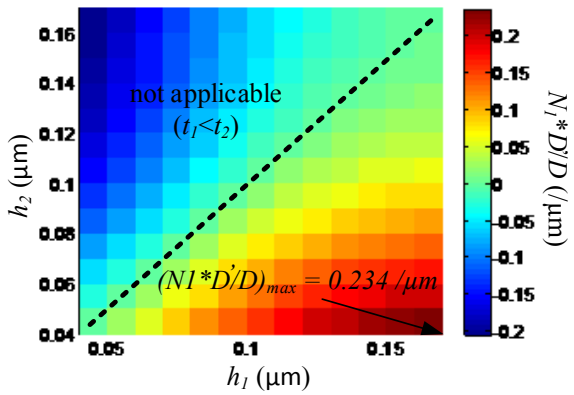

Fig. 8 Value of the quantity R as a function of layer thicknesses h_1 and h_2.

2. Fig. 9 shows the modal transmittance at the adiabatic interface, of which the structural parameters are given in the inset, as a function of the angle of incidence (from the high thickness side), as calculated by transforming the 3-D scattering problem (scalar approximation) to an effective 2-D Helmholtz problem [2, 17], where the incidence angle appears as a parameter. This effective equation is then solved by a quasi-analytic 2-D method,

applying a fine staircase approximation of the taper profile [18]. Owing to the adiabaticity the curve changes abruptly from nearly unity to zero at an angle equal to θ_{crit}. The angle σ is chosen somewhat below θ_{crit}, at $\sigma = \theta_{crit} - 5°$. This choice leads to $\eta = 142.7°$, $\sigma_2' = 0.4072\ \mathrm{rad/\mu m}$ (see Sec. 2.1). The smallest angle of incidence on the mirror is chosen as $\theta_l = \theta_{crit} + 1°$.

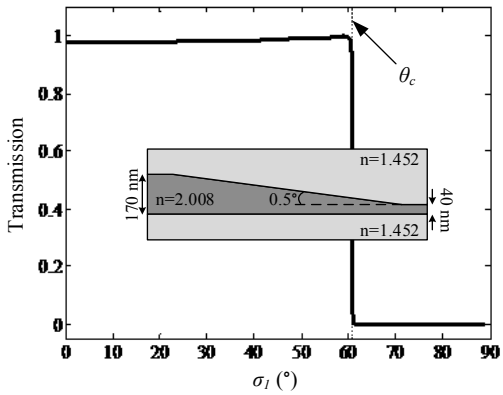

Fig. 9 Transmittance vs. angle of incidence on the adiabatic taper. The inset depicts the taper structure.

3. Considering Fig. 5 (a) and Fig. 5 (b) with the above performance conditions in mind it is seen that the combination $V = 6$ and $\varsigma = 3$ fulfills all the requirements: the ACCT (=$O(t/w_O = 2)$) is well below $-40\ dB$ and the global CT is sufficiently low. A combination of $V \geq 6$ and $\varsigma = 2$ would also be suitable and lead to a comparable device area, but the losses will be a bit higher, ~4% according to Fig. 5 (d). From the formulae presented earlier, it now follows: $w_O = 3.74\ \mu m$ (from Fig. 5 (d)), $f = 3.674\ mm$ (from Eq. (32)), $W = 307\ \mu m$ and $B = 921\ \mu m$ (from Eq. (29)) and $\gamma = 14.34°$. Note that, as a consistency check, f also has been calculated using both the formula $\tilde{B} = f\gamma$ and the geometrical parameters of the mirror; it was found that all three approaches led to the same result.

4. We propose a new method to calculate the PSR at slab waveguide interfaces [17]. In this method an imaginary waveguide structure with symmetric tapered edges, which are identical to the tapered profiles to be used in the mirror and prism interfaces, is considered. Fig. 10 shows the structure of this imaginary waveguide, which is a ridge waveguide with $40\ nm$ (equal to prism slab thickness) and $170\ nm$ (equal to field slab thickness) slab waveguide thicknesses and the taper between these thicknesses has an angle of 0.5°, as defined by the fabrication process. Analysis of the field of the channel mode in the center of the imaginary waveguide shows that it is composed of virtually only the TE slab mode for not too narrow channel waveguides, i.e., the overlap between this field and the $170\ nm$ thick slab mode is close to unity. Therefore, the structure can be pictured as a simple waveguide in which the TE slab mode is bouncing between the tapered edges (see Fig. 11).

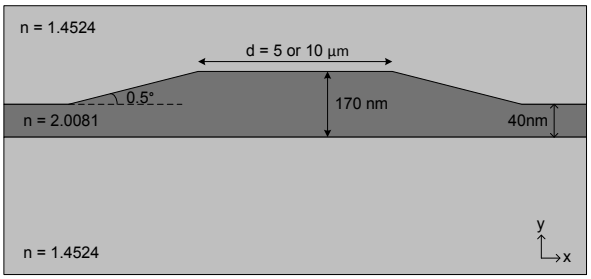

Fig. 10 Structure of the imaginary channel waveguide used to calculate phase change upon total internal reflection of slab TE modes.

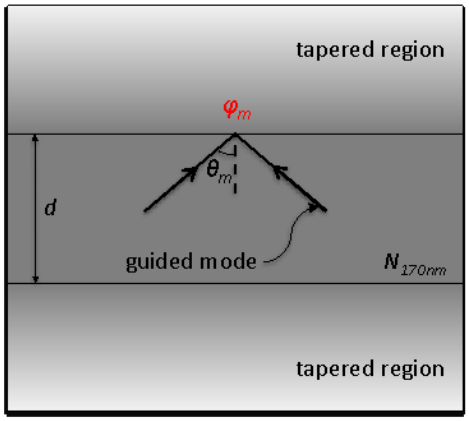

Fig. 11 Simplified 1D view of the imaginary waveguide structure.

In order to find the numerical values of the PSR as a function of the angle of incidence, θ, the transverse resonance condition can be used

$$2dN_{170nm}\frac{2\pi}{\lambda}\cos\theta_m - 2\varphi_m = m2\pi, \tag{38}$$

where m denotes the mode number, d is the width of the non-tapered waveguide part, N_{170nm} is the effective index of the 170 nm slab. The mode angle, θ_m, for a specific channel mode can be calculated by using the following formula;

$$N_m = N_{170nm}\sin\theta_m, \tag{39}$$

where N_m is the effective index of the m^{th} channel waveguide mode, calculated using appropriate software. For each channel mode one thus obtains a sample value φ_m for the PSR of the incidence angle θ_m by using Eq. (38). Fig. 12 shows the calculated phase shift upon TIR at the considered tapered interface for two different non-tapered waveguide widths (d) at $\lambda = 850\ nm$ for a number of angles of incidence and the polynomial fit of the data for $d = 5\ \mu m$. The incidence angle range ($\Delta\theta$) used in the designed mirror is also depicted in the figure. It can be seen from the figure that the results for different d values are in good agreement. θ_m values of the data points on this figure correspond to discrete channel waveguide modes. In order to calculate a smooth curve $\varphi(\theta)$ these data points can be fitted to a polynomial function. Knowing the relation $\varphi(\theta)$ the full layout of the spectrometer can be designed using ray tracing together with Eqs. (34) and (36), to account for the and GHS. In order to give some feeling about the magnitude of these effects in the mirror that has an adiabatic interface with 0.5° as depicted in Fig. 10, we present the induced deflection angle and the GHS for the central ray hitting the mirror being: $\Psi = 0.32°$ (calculated using Eq. (35)) and GHS = 83.77 μm (calculated using Eq. (36)), respectively.

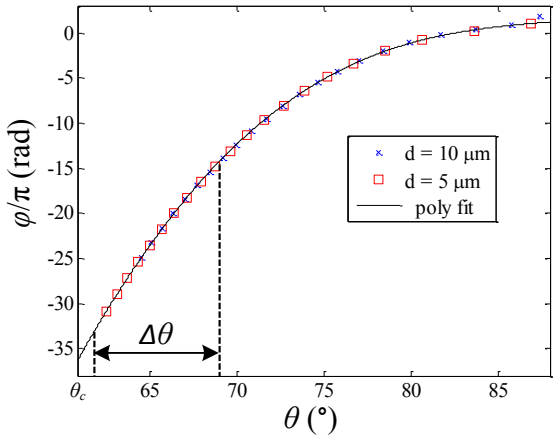

Fig. 12 Phase shift upon TIR vs. incidence angle for the considered interface with 0.5° taper angle at λ = 850 nm. $\Delta\theta$ is the used incidence angle range for the designed mirror.

As an example of the effect of the applied correction for waveguide positions we present some results calculated using ray tracing based numerical calculations, in which a set of parallel rays propagating in the x direction (see Fig. 3) hit the parabolic mirror and converge on a point (correct position of the waveguide) by taking into account the varying (with angle and position) PSR. As a result, the input waveguide has to be shifted $74.9\ \mu m$ in positive x direction, $29.7\ \mu m$ in positive y direction and turned by $0.64°$ ($0.011\ rad$) CCW. For the receiver waveguides the effect corresponds to a considerable wavelength shift being $(0.011/\sigma_2' =)\ 27.38\ nm$.

5. With geometrical optics we have, for the structure resulting from the above steps, calculated the broadening of the image field for the outermost wavelengths of the considered region ($\lambda = 800$ and $900\ nm$). Considering only the rays in-between the two rays corresponding to the FWHM of the field coming from the focusing mirror (representing the major part of the power of the beam) a focal spot broadening of $0.6\mu m$ was found. This is equal to around 20.1% of the un-blurred image implying an approximate broadening as small as 2% ($\sqrt{1+0.2^2}-1=0.02$) and a minor extra functional loss of around 1%. Here we assumed for simplicity Gaussian shapes for the beam cross section and the broadening. So, the aberration effect is minor and requires no structural adaptations. The resulting layout of the spectrometer is presented in Fig. 13. The size of the device is $5.5\ x\ 13\ mm^2$ including the input and output waveguides. These dimensions are much smaller than the size of a comparable AWG device, which has a resolution of 5.5 nm (very close to the resolution of proposed device) and implemented in SiON technology, being $50\ x\ 20\ mm^2$ [19]. Therefore the propagation losses will be lower in the proposed device. Furthermore, we think that the scattering losses will be less significant in our device since it suffers less from sidewall roughness occurring in channel waveguides (in the presented device the light propagates mainly in slab waveguide regions rather than in channel waveguides).

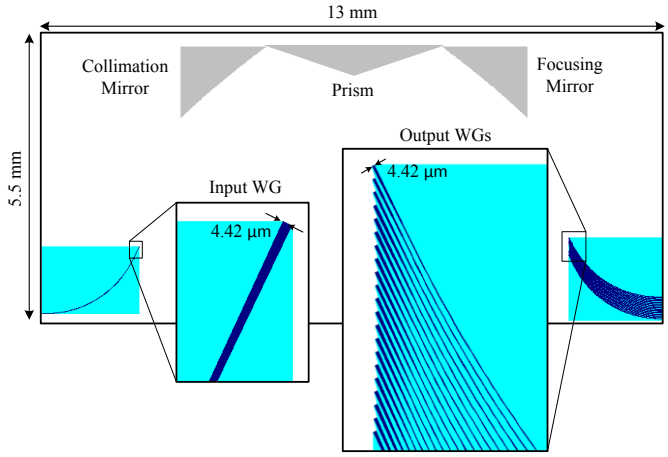

Fig. 13 Full layout of the designed prism spectrometer, which has a size of $5.5\ x\ 13\ mm^2$; the inset shows the input and receiver waveguides in more detail.

4. CONCLUSION

We have presented a general approach for the design of a planar prism-based spectrometer, utilizing dispersion effects in two slab waveguiding areas having different thicknesses of the guiding layer. Here, the different regions are assumed to be adiabatically connected via vertical tapering. Part of the design strategy is generally applicable and can be used for also for the design of for example arrayed waveguide gratings. A new method to cope with the effect of both angle of incidence and position dependent modal phase shifts upon modal reflection by (parabolic) mirrors, defined by the interface between areas of different slab thicknesses, has been presented.

The design strategy was illustrated by a numerical example assuming SiON technology. Assuming a central wavelength of 850 nm, a 3 dB bandwidth, a channel spacing of $5\ nm$, an adjacent channel cross talk of $-40\ dB$ and a cross talk of $-50\ dB$ lead to a required device area of $5.5\ x\ 13\ mm^2$ and a minor functional loss of a few percent over a wavelength range of $100nm$.

ACKNOWLEDMENT

This work was supported by the Dutch Technology Foundation STW through the project Optical Lab in a Package (10051). M. Hammer acknowledges financial support by the German Research Foundation (Deutsche Forschungsgemeinschaft DFG, project HA7314/1-1)

REFERENCES

[1] P. Tien, Integrated optics and new wave phenomena in optical waveguides, Reviews of Modern Physics. 49 (1977) 361-420.

[2] R. Martin, R. Ulrich, Geometrical optics in thin film light guides, Applied Optics. 10 (1971) 2077-2085.

[3] C. Tseng, W. Tsang, S. Wang, A thin-film prism as a beam seperator for multimode guided waves in integrated optics, Optics Communications. 13 (1975) 342-346.

[4] M. Gibbon, G. Thompson, S. Clements, D. Moule, C. Rogers, C. Cureton, Optical performance of integrated 1.5 um grating wavelength-demultiplexer on InP-based waveguide, Electronics Lett. 25 (1989) 1441-1442.

[5] C. Chen, R. Jang, Polymer-based 1x6 thermooptic switch incorporating an elliptic TIR waveguide mirror, Journal of Ligthtwave Technology. 21 (2003) 1053-1058.

[6] M.K. Smit, C. van Dam, Phasar-based WDM-devices: Principles, design and applications, IEEE J. Selected Topics in Quant. Electron. 2 (1996) 236-250.

[7] N. Ismail, F. Sun, G. Sengo, K.Wörhoff, A. Driessen, R. de Ridder, M.Pollnau, Improved arrayed waveguide grating layout avoiding systematic phase errors, Optics Express. 19 (2011) 8781-8794.

[8] B.I. Akça, V. Duc Nguyen, J. Kalkman, N. Ismail, G. Sengo, Fei Sun, A. Driessen, T.G. van Leeuwen, M. Pollnau, K. Wörhoff, R.M. de Ridder, Toward spectral-domain optical coherence tomography on a chip, IEEE Journal of Selected Topics in Quantum Electronics. 18 (2012) 1223-1233.

[9] S. Janz, A. Balakrishnan, S. Charbonneau, P. Cheben, M. Cloutier, A. Delâge, K. Dossou, L. Erickson, M. Gao, P.A. Krug, B. Lamontagne, M. Packirisamy, M. Person, D.-X. Xu, Planar waveguide Echelle gratings in Silica-on Silicon, IEEE Photon. Electron. Lett. 16 (2004) 503-505.

[10] P.J. Bock, P. Cheben, J.H. Schmid, A.V. Velasco, A. Delâge, S. Janz, D.-X. Xu, J. Lapointe, T.J. Hall, M.L. Calvo, Demonstration of a curved sidewall grating demultiplexer on silicon, Opt. Express. 20 (2012) 19882-19892.

[11] Y. Zhang, W. Huang, X. Wang, H. Xu, Z. Cai, A novel super-high extinction ratio comb-filter based on cascaded Mach-Zehnder Gires-Tournois interferometers with dispersion compensation, Opt. Express. 17 (2009) 13685-13699.

[12] F. Xia, M. Rooks, L. Sekaric, Y. Vlasov, Ultra-compact high order ring resonator filters using submicron silicon photonic wires for on-chip optical interconnects, Opt. Express. 19 (2007) 11934–11941.

[13] F. Civitci, Integrated optical modules for miniature Raman spectroscopy devices, PhD. thesis, University of Twente, Enschede, 2014.

[14] K.R. Williams, R.S. Muller, Etch rates for micromachining processing, Journal of Micro-electromechanical Systems, 5 (1996) 256-269.

[15] E. Hecht, Optics, fourth ed., Addison-Wesley, New York, 2002.

[16] H. Kogelnik, Theory of optical waveguides, in: T. Tamir (Ed.), Guided-wave Optoelectronics, Springer Verlag, Berlin, 1988, pp. 7-88.

[17] F. Civitci, M. Hammer, H.J.W.M. Hoekstra, Semi-guided plane wave reflection by thin-film transitions for angled incidence, Optical and Quantum Electronics. 46 (2014) 477-490.

[18] M. Hammer, Quadridirectional eigenmode expansion scheme for 2D modeling of wave propagation in integrated optics, Optical Communications. 235 (2004) 285–303.

[19] N. Ismail, F. Sun, G. Sengo, K. Wörhoff, A. Driessen, R. de Ridder, M. Pollnau, Improved arrayed-waveguide-grating layout avoiding systematic phase errors, Optics Express 19 (2011) 8781-8794.